HAL
open science

Fully automated digital holographic processing for monitoring the dynamics of a vesicle suspension under shear flow

Christophe Minetti, Thomas Podgorski, Gwennou Coupier, Frank Dubois

To cite this version:

Christophe Minetti, Thomas Podgorski, Gwennou Coupier, Frank Dubois. Fully automated digital holographic processing for monitoring the dynamics of a vesicle suspension under shear flow. Biomedical optics express, 2014, 5, pp.1554-1568. 10.1364/BOE.5.001554 . hal-00980352

HAL Id: hal-00980352

https://hal.univ-grenoble-alpes.fr/hal-00980352v1

Submitted on 17 Apr 2014

HAL is a multi-disciplinary open access archive for the deposit and dissemination of scientific research documents, whether they are published or not. The documents may come from teaching and research institutions in France or abroad, or from public or private research centers.

L'archive ouverte pluridisciplinaire **HAL**, est destinée au dépôt et à la diffusion de documents scientifiques de niveau recherche, publiés ou non, émanant des établissements d'enseignement et de recherche français ou étrangers, des laboratoires publics ou privés.

Biomedical Optics EXPRESS

Fully automated digital holographic processing for monitoring the dynamics of a vesicle suspension under shear flow

Christophe Minetti,[1,*] Thomas Podgorski,[2] Gwennou Coupier,[2] and Frank Dubois[1]

[1]*Service de Chimie-Physique EP, Université libre de Bruxelles, 50 Avenue F. Roosevelt, CP16/62, B-1050 Brussels, Belgium*

[2]*Laboratoire Interdisciplinaire de Physique, CNRS-UMR 5588, Université Grenoble I, B.P. 87, 38402 Saint Martin d'Hères Cedex, France*

[*]*cminetti@ulb.ac.be*

Abstract: We investigate the dynamics of a vesicle suspension under shear flow between plates using DHM with a spatially reduced coherent source. Holograms are grabbed at a frequency of 24 frames/sec. The distribution of the vesicle suspension is obtained after numerical processing of the digital holograms sequence resulting in a 4D distribution. Obtaining this distribution is not straightforward and requires special processing to automate the analysis. We present an original method that fully automates the analysis and provides distributions that are further analyzed to extract physical properties of the fluid. Details of the numerical implementation, as well as sample experimental results are presented.

©2014 Optical Society of America

OCIS codes: (090.0090) Holography; (100.0100) Image processing; (090.1995) Digital holography; (100.2000) Digital image processing; (100.6890) Three-dimensional image processing; (170.6900) Three-dimensional microscopy.

References and links

1. C. Minetti and C. Buffone, "Three-dimensional Marangoni cell in self-induced evaporating cooling unveiled by digital holographic microscopy," Phys. Rev. E Stat. Nonlin. Soft Matter Phys. **89**(1), 013007 (2014).
2. Y. Yang, G. Li, L. Tang, and L. Huang, "Integrated gray-level gradient method applied for the extraction of three-dimensional velocity fields of sprays in in-line digital holography," Appl. Opt. **51**(2), 255–267 (2012).
3. I. Moon, B. Javidi, F. Yi, D. Boss, and P. Marquet, "Automated statistical quantification of three-dimensional morphology and mean corpuscular hemoglobin of multiple red blood cells," Opt. Express **20**(9), 10295–10309 (2012).
4. I. Moon, F. Yi, Y. H. Lee, B. Javidi, D. Boss, and P. Marquet, "Automated quantitative analysis of 3D morphology and mean corpuscular hemoglobin in human red blood cells stored in different periods," Opt. Express **21**(25), 30947–30957 (2013).
5. D. Carl, B. Kemper, G. Wernicke, and G. von Bally, "Parameter-optimized digital holographic microscope for high-resolution living-cell analysis," Appl. Opt. **43**(36), 6536–6544 (2004).
6. L. Miccio, A. Finizio, R. Puglisi, D. Balduzzi, A. Galli, and P. Ferraro, "Dynamic DIC by digital holography microscopy for enhancing phase-contrast visualization," Biomed. Opt. Express **2**(2), 331–344 (2011).
7. Y.-S. Choi and S.-J. Lee, "Three-dimensional volumetric measurement of red blood cell motion using digital holographic microscopy," Appl. Opt. **48**(16), 2983–2990 (2009).
8. A. El Mallahi, C. Minetti, and F. Dubois, "Automated three-dimensional detection and classification of living organisms using digital holographic microscopy with partial spatial coherent source: Application to the monitoring of drinking water resources," Appl. Opt. **52**(1), A68–A80 (2013).
9. R. Liu, D. K. Dey, D. Boss, P. Marquet, and B. Javidi, "Recognition and classification of red blood cells using digital holographic microscopy and data clustering with discriminant analysis," J. Opt. Soc. Am. A **28**(6), 1204–1210 (2011).
10. P. Memmolo, M. Iannone, M. Ventre, P. A. Netti, A. Finizio, M. Paturzo, and P. Ferraro, "On the holographic 3D tracking of in vitro cells characterized by a highly-morphological change," Opt. Express **20**(27), 28485–28493 (2012).
11. F. Dubois, L. Joannes, and J.-C. Legros, "Improved three-dimensional imaging with a digital holography microscope with a source of partial spatial coherence," Appl. Opt. **38**(34), 7085–7094 (1999).
12. F. Dubois, M. L. Requena, C. Minetti, O. Monnom, and E. Istasse, "Partial spatial coherence effects in digital holographic microscopy with a laser source," Appl. Opt. **43**(5), 1131–1139 (2004).
13. J.-M. Poiseuille, C. R. Hebd. Seances Acad. Sci. **1**, 554 (1835).

#206641 - $15.00 USD Received 18 Feb 2014; revised 10 Apr 2014; accepted 11 Apr 2014; published 17 Apr 2014

14. N. Callens, C. Minetti, G. Coupier, M.-A. Mader, F. Dubois, C. Misbah, and T. Podgorski, "Hydrodynamical lift of vesicles undear shear flow in microgravity," Europhys. Lett. **83**(2), 24002 (2008).
15. C. Minetti, N. Callens, G. Coupier, T. Podgorski, and F. Dubois, "Fast measurements of concentration profiles inside deformable objects in microflows with reduced spatial coherence digital holography," Appl. Opt. **47**(29), 5305–5314 (2008).
16. V. Vitkova, M.-A. Mader, B. Polack, C. Misbah, and T. Podgorski, "Micro-macro link in rheology of erythrocyte and vesicle suspensions," Biophys. J. **95**(6), L33–L35 (2008).
17. K. H. de Haas, C. Blom, D. van den Ende, M. H. G. Duits, B. Haveman, and J. Mellema, "Rheological behavior of a dispersion of small lipid bilayer vesicles," Langmuir **13**(25), 6658–6668 (1997).
18. M. Abkarian, C. Lartigue, and A. Viallat, "Tank Treading and Unbinding of Deformable Vesicles in Shear Flow: Determination of the Lift Force," Phys. Rev. Lett. **88**(6), 068103 (2002).
19. V. Kantsler, E. Segre, and V. Steinberg, "Dynamics of interacting vesicles and rheology of vesicle suspension in shear flow," Europhys. Lett. **82**(5), 58005 (2008).
20. G. Coupier, B. Kaoui, T. Podgorski, and C. Misbah, "Noninertial lateral migration of vesicles in bounded Poiseuille flow," Phys. Fluids **20**(11), 111702 (2008).
21. J. Deschamps, V. Kantsler, and V. Steinberg, "Phase Diagram of Single Vesicle Dynamical States in Shear Flow," Phys. Rev. Lett. **102**(11), 118105 (2009).
22. J. Deschamps, V. Kantsler, E. Segre, and V. Steinberg, "Dynamics of a vesicle in general flow," Proc. Natl. Acad. Sci. U.S.A. **106**(28), 11444–11447 (2009).
23. H. Noguchi, G. Gompper, L. Schmid, A. Wixforth, and T. Franke, "Dynamics of fluid vesicles in flow through structured microchannels," Europhys. Lett. **89**(2), 28002 (2010).
24. G. Coupier, A. Farutin, C. Minetti, T. Podgorski, and C. Misbah, "Shape Diagram of Vesicles in Poiseuille Flow," Phys. Rev. Lett. **108**(17), 178106 (2012).
25. M. Levant, J. Deschamps, E. Afik, and V. Steinberg, "Characteristic spatial scale of vesicle pair interactions in a plane linear flow," Phys. Rev. E Stat. Nonlin. Soft Matter Phys. **85**(5), 056306 (2012).
26. P.-Y. Gires, A. Srivastav, C. Misbah, T. Podgorski, and G. Coupier, "Pairwise hydrodynamic interactions and diffusion in a vesicle suspension," Phys. Fluids **26**(1), 013304 (2014).
27. P. Olla, "The Lift on a Tank-Treading Ellipsoidal Cell in a Shear Flow," J. Phys. II **7**(10), 1533–1540 (1997).
28. V. V. Lebedev, K. S. Turitsyn, and S. S. Vergeles, "Dynamics of Nearly Spherical Vesicles in an External Flow," Phys. Rev. Lett. **99**(21), 218101 (2007).
29. G. Danker and C. Misbah, "Rheology of a Dilute Suspension of Vesicles," Phys. Rev. Lett. **98**(8), 088104 (2007).
30. B. Kaoui, G. Biros, and C. Misbah, "Why Do Red Blood Cells Have Asymmetric Shapes Even in a Symmetric Flow?" Phys. Rev. Lett. **103**(18), 188101 (2009).
31. H. Zhao, A. Spann, and E. S. G. Shaqfeh, "The dynamics of a vesicle in a wall-bound shear flow," Phys. Fluids **23**(12), 121901 (2011).
32. T. Biben, A. Farutin, and C. Misbah, "Three-dimensional vesicles under shear flow: Numerical study of dynamics and phase diagram," Phys. Rev. E Stat. Nonlin. Soft Matter Phys. **83**(3), 031921 (2011).
33. A. Farutin and C. Misbah, "Squaring, Parity Breaking, and S Tumbling of Vesicles under Shear Flow," Phys. Rev. Lett. **109**(24), 248106 (2012).
34. A. Farutin and C. Misbah, "Rheology of vesicle suspensions under combined steady and oscillating shear flows," J. Fluid Mech. **700**, 362–381 (2012).
35. G. Boedec, M. Jaeger, and M. Leonetti, "Settling of a vesicle in the limit of quasispherical shapes," J. Fluid Mech. **690**, 227–261 (2012).
36. A. Farutin and C. Misbah, "Analytical and Numerical Study of Three Main Migration Laws for Vesicles Under Flow," Phys. Rev. Lett. **110**(10), 108104 (2013).
37. D. Abreu and U. Seifert, "Noisy Nonlinear Dynamics of Vesicles in Flow," Phys. Rev. Lett. **110**(23), 238103 (2013).
38. H. Zhao and E. S. G. Shaqfeh, "The dynamics of a non-dilute vesicle suspension in a simple shear flow," J. Fluid Mech. **725**, 709–731 (2013).
39. T. Podgorski, N. Callens, C. Minetti, G. Coupier, F. Dubois, and C. Misbah, "Dynamics of vesicle suspension in shear flow between walls," Microgravity Sci. Technol. **23**(2), 263–270 (2011).
40. A. S. Popel and P. C. Johnson, "Microcirculation and hemorheology," Annu. Rev. Fluid Mech. **37**(1), 43–69 (2005).
41. M. I. Angelova, S. Soleau, P. Meleard, J.-F. Faucon, and P. Bothorel, "Preparation of giant vesicles by external A.C. electric fields. Kinetics and applications," Prog. Colloid Polym. Sci. **89**, 127 (1992).
42. J. Gao, D. R. Guildenbecher, P. L. Reu, and J. Chen, "Uncertainty characterization of particle depth measurement using digital in-line holography and the hybrid method," Opt. Express **21**(22), 26432–26449 (2013).
43. D. R. Guildenbecher, J. Gao, P. L. Reu, and J. Chen, "Digital holography simulations and experiments to quantify the accuracy of 3D particle location and 2D sizing using a proposed hybrid method," Appl. Opt. **52**(16), 3790–3801 (2013).
44. T. Kreis, "Digital holographic interference phase measurement using the Fourier-transform method," J. Opt. Soc. Am. A **3**(6), 847–855 (1986).
45. M. Takeda, H. Ina, and S. Kobayashi, "Fourier-transform method of fringe pattern analysis for computer-based topography and interferometry," J. Opt. Soc. Am. **72**(1), 156–180 (1982).
46. D. C. Ghigliz and M. D. Pritt, Two-Dimensional Phase unwrapping. Theory, Algorithms, and Sofware (Wiley-Interscience 1998).

#206641 - $15.00 USD Received 18 Feb 2014; revised 10 Apr 2014; accepted 11 Apr 2014; published 17 Apr 2014

47. T. Colomb, F. Montfort, J. Kühn, N. Aspert, E. Cuche, A. Marian, F. Charrière, S. Bourquin, P. Marquet, and C. Depeursinge, "Numerical parametric lens for shifting, magnification, and complete aberration compensation in digital holographic microscopy," J. Opt. Soc. Am. A **23**(12), 3177–3190 (2006).
48. P. Ferraro, D. Alferi, S. De Nicola, L. De Petrocellis, A. Finizio, and G. Pierattini, "Quantitative phase-contrast microscopy by a lateral shear approach to digital holographic image reconstruction," Opt. Lett. **31**(10), 1405–1407 (2006).
49. F. Dubois, O. Monnom, C. Yourassowsky, and J.-C. Legros, "Border processing in digital holography by extension of the digital hologram and reduction of the higher spatial frequencies," Appl. Opt. **41**(14), 2621–2626 (2002).
50. F. Dubois, C. Schockaert, N. Callens, and C. Yourassowsky, "Focus plane detection criteria in digital holography microscopy by amplitude analysis," Opt. Express **14**(13), 5895–5908 (2006).
51. A. El Mallahi and F. Dubois, "Separation of overlapped particles in digital holographic microscopy," Opt. Express **21**(5), 6466–6479 (2013).
52. A. El Mallahi and F. Dubois, "Dependency and precision of the refocusing criterion based on amplitude analysis in digital holographic microscopy," Opt. Express **19**(7), 6684–6698 (2011).
53. D. Mumford and J. Shah, "Optimal approximation by piece-wise smooth functions and associated variational problems," Commun. Pure Appl. Math. **42**(5), 577–685 (1989).
54. O. Monnom, F. Dubois, C. Yourassowsky, and J. C. Legros, "Improvement in visibility of an in-focus reconstructed image in digital holography by reduction of the influence of out-of-focus objects," Appl. Opt. **44**(18), 3827–3832 (2005).
55. X. Grandchamp, G. Coupier, A. Srivastav, C. Minetti, and T. Podgorski, "Lift and down-gradient shear-induced diffusion in red blood cell suspensions," Phys. Rev. Lett. **110**(10), 108101 (2013).
56. A. Srivastav, T. Podgorski, and G. Coupier, "Efficiency of size-dependent particle separation by pinched flow fractionation," Microfluid. Nanofluid. **13**(5), 697–701 (2012).
57. M. Yamada, M. Nakashima, and M. Seki, "Pinched flow fractionation: Continuous size separation of particles utilizing a laminar flow profile in a pinched microchannel," Anal. Chem. **76**(18), 5465–5471 (2004).
58. F. Da Cunha and E. Hinch, "Shear-induced dispersion in a dilute suspension of rough spheres," J. Fluid Mech. **309**(-1), 211–223 (1996).
59. R. E. Pattle, "Diffusion from an instantaneous point source with a concentration-dependent coefficient," Q. J. Mech. Appl. Math. **12**(4), 407–409 (1959).

1. Introduction

Optical microscopy is limited by the small depths of focus due to high numerical apertures and the high magnification ratios. The extension of the depth of focus has become an important goal in optical microscopy. In this way, Digital Holographic Microscopy (DHM) provides a natural and elegant solution to this problem by giving the capability to reconstruct numerically different slices inside an experimental volume. On the basis of the knowledge of the complex amplitude in one plane, one can easily propagate this complex amplitude to different planes along the optical axis by implementing numerically the propagation equations of Kirchhoff-Fresnel. Furthermore, DHM provides a quantitative optical phase which is particularly useful for pure phase objects (like living cells). DHM has been successfully used for different applications in fluid physics [1,2] but also in biological applications such as living cell culture monitoring, observation of biological samples [3–7], classification of microscopic living organisms [8,9], living cells tracking [10. For the last decade, we have developed DHM working with reduced spatial coherent sources [11]. It has been shown that the reduction of the spatial coherence strongly improves the quality of the holograms [12], especially when the experimental cell under investigation cannot be optimized with respect to the optical quality. DHM can be a powerful measuring instrument but is often problem dependent and requires the implementation of specific holographic information processing techniques.

Channel flows of complex fluids containing deformable particles such as Red Blood Cells (RBCs) are influenced by many phenomena such as hydrodynamic interactions between particles and between channel walls and particles, phase separation at bifurcations, which all depend on the mechanical properties of the particles. While blood flows have been observed for nearly two centuries [13], their understanding is still incomplete. In particular, understanding the concentration inhomogeneities between vessels or across one given vessel, or the interplay between RBCs, White Blood Cells an platelets still requires huge efforts from the community, in terms of experiments or numerical simulations.

Significant advances in the investigation of the physical mechanisms leading to the structuring of blood in flow has been made over the past years through the use of models like

#206641 - $15.00 USD Received 18 Feb 2014; revised 10 Apr 2014; accepted 11 Apr 2014; published 17 Apr 2014

giant lipid vesicles (closed lipid bilayers enclosing a fluid). Since they retain the main mechanical characteristics of RBCs with a reduced set of easily controlled parameters, they have been the subject of many experimental [14–26] and numerical/theoretical investigations [24,26–38].

Two phenomena are of particular interest in confined shear-flow in the understanding of blood rheology: when sheared close to a wall, deformable objects such as vesicles or RBCs undergo a lift force of viscous origin which pushes them away from walls [14,18,39] while on the other hand hydrodynamic interactions and collisions within the suspension lead to shear-induced diffusion that tends to homogenize the concentration. When these two effects balance, a cell-free layer is formed near walls and plays a decisive role in biological functions (cell adhesion and aggregation, immunitary response, rheology of blood in confined situations [40]) and may be of interest in technological applications such as cell sorting devices, etc…

In this paper, we aim at describing an automated protocol to study the 4D behavior of a vesicle suspension in flow. We illustrate the procedure by shearing a suspension between two plates. The bottom plate is fixed while the top one is rotating creating a linear profile of velocity of the fluid between the plates. The thickness of the channel is about 200 µm. The distribution of the vesicle suspension over the thickness of the channel is obtained by monitoring the suspension with a spatially reduced coherence DHM. Depending on the concentration of the samples, the duration of the experiments (between 20 and 100 sec at 24 frames/sec), the number of experiments needed to get reliable statistical data, the different experimental parameters to be investigated etc … the number of holograms to be processed becomes rapidly huge and there is a real need to automate the processing. This automation is not straightforward as it requires detecting the tri-dimensional position of each vesicle present in the field of view but also specific features such as its size and shape. The proposed technique combines several algorithms in an original way. Because vesicles are pure phase objects, they become invisible when they are in the focus plane. To solve the problem, we take benefit of the full interferometric information by working on the intensity image and especially on the phase map provided quantitatively by DHM.

The optical system is briefly described in section 2. The experimental protocol is detailed in section 3. Section 4 reports the processing sequence of the holograms. Illustrative examples are given in section 5 and concluding remarks in section 6.

2. Optical setup description

This section describes the DHM setup used for the experiments. The optical setup is described in Fig. 1. It is a Mach-Zehnder configuration with microscope lenses (x20) to provide the magnification. The interferometer is using a reduced spatial coherent source provided by a laser source (monomode laser diode, λ = 635 nm) focused by lens L1 on a rotating ground glass (RGG). By adjusting the position of the rotating ground glass on the optical axis, one can easily increase the spatial extension of the source and consequently decrease the spatial coherence.

#206641 - $15.00 USD Received 18 Feb 2014; revised 10 Apr 2014; accepted 11 Apr 2014; published 17 Apr 2014
(C) 2014 OSA

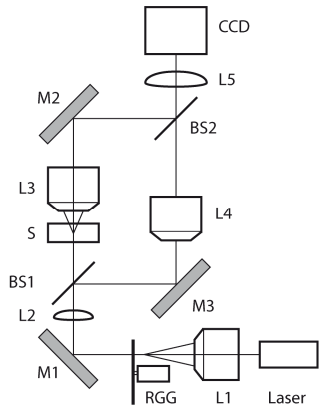

Fig. 1. Optical setup description. L1, focusing lens; RGG, Rotating Ground Glass for spatial coherence reduction; L2, collimating lens; L3, L4, identical microscope lenses (x20); L5, refocusing lens; CCD, charge-coupled device camera; M1-M3, mirrors; BS1, BS2, beam splitters; S, sample.

The use of spatial coherence reduces the coherent noise and provides a temporal-like effect that eliminates the coherent multiple reflection issue [12]. Holograms are acquired with a charge-coupled device (CCD) camera. We used a JAI CV-M4 camera with an array of 1280 x 1024 pixels corresponding to an optical field of view of 524 µm x 420 µm. The angle between the reference and the object beam (passing through the sample) is adjusted to work in an off-axis configuration allowing a fast acquisition (24 frames/sec) with a very short exposure time (200 µm) and avoid blurring when using high flow rates.

3. Objective and experimental protocol

The main objective of the experiment is to get dynamic properties of a vesicle suspension under shear flow. As outlined in the introduction, two physical effects govern the behavior of the suspension: a lift force due to the presence of walls and shear induced diffusion due to interactions between vesicles. At shear rates relevant to practical situations, sedimentation cannot be neglected and significantly affects the results. To remove the screening effects of gravity (the sedimentation speed of vesicles is of the same order as the lift velocity we investigate), experiments were conducted in microgravity (on parabolic flight and in sounding rockets) with a Couette shear flow chamber designed and manufactured by the Swedish Space Corporation (SSC). As shown in Fig. 2, it is made of two parallel glass discs, with a diameter of 10 cm and a gap of 170 µm.

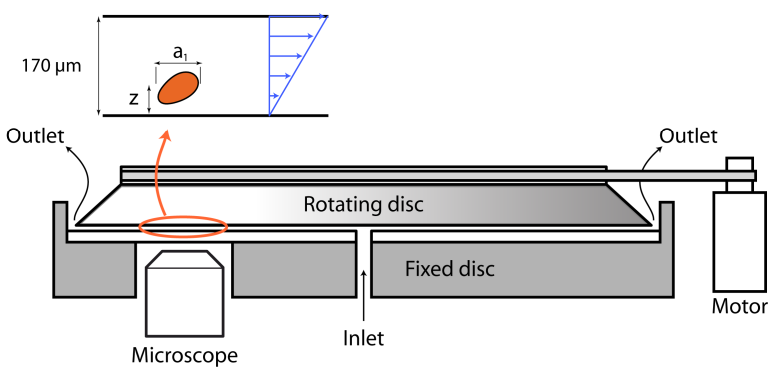

Fig. 2. Sketch of the experimental shear flow chamber.

#206641 - $15.00 USD Received 18 Feb 2014; revised 10 Apr 2014; accepted 11 Apr 2014; published 17 Apr 2014

An inlet at the center of the bottom plate and several outlets at the periphery allow filling with experimental fluids, vesicle injection and rinsing. Vesicle suspensions and extra carrier fluid (to control the concentration of the samples by dilution) are contained in syringes (mounted on a syringe pump) to the inlet via flexible tubes.

Vesicles were prepared by the electroformation method [41] from lipids (1,2 – Dioleoyl-sn-glycero-3-Phosphocholine (DOPC)) deposited on ITO glass plates and a solution to be encapsulated made of 80% water and 20% glycerol w:w, where 300 mM of sucrose are dissolved. Each electroformation provides a polydisperse sample with vesicles diameter ranging from 5 to 100 µm (median size between 15 and 25 µm), a volume fraction of a few percent and a total volume of 2 ml. Samples were then diluted into a slightly hyperosmotic solution made of 80% water and 20% glycerol w:w, and 350 mM of glucose creating a refractive index change Δn of 0.0061.

4. Digital processing of numerical holograms

Digital holograms are grabbed and stored on a hard disk for further processing. The huge amount of data stored requires a fully automated processing minimizing any intervention of an operator and getting the maximum reliability of the processing. Automated three-dimensional detection is generally problem dependent and there is no miracle solution that solves the automatic detection problem. Different methods have been proposed based on the accumulation of interferometric information during the numerical propagation along the optical axis [8,42,43].

The processing sequence can be summarized as follow: for each hologram, find the position, the size and the shape of each vesicle present in the considered hologram. In the following, we will consider the processing of one hologram, all the holograms of the sequence are processed in the same way and do not depend on their temporal position in the sequence. The very first step is to extract the complex amplitude $U(x,y) = A(x,y)exp(i\phi(x,y))$ (amplitude $A(x,y)$ and phase $\phi(x,y)$, i being the imaginary number) from the hologram using the Fourier method [43–45]. On the basis of the complex amplitude $U(x,y)$, the task can be divided in two parts: first find the position xyz of each vesicle; secondly extract the features of each vesicle in its corresponding z plane. Those two operations are described in details in the following subsections.

4.1 Automatic XYZ detection

Vesicles are pure phase objects becoming transparent in intensity when they are in the focus plane. Intuitively, one can easily understand that in the vicinity of a vesicle, the xy gradient is minimal at the focus plane. This property could be exploited to scan the experimental volume along the z direction and, for each plane, compute the xy gradient of the reconstructed intensity. The xyz detection of the vesicles would then be performed by thresholding the different gradient of intensity in the different reconstructed planes. This approach is intuitively attractive but suffers from two drawbacks. First, it requires propagating the whole hologram along the z axis (covering the whole experimental volume) with a sufficiently small increment Δz to detect the smallest vesicles. This becomes rapidly heavy in computation time. Secondly, the method is very sensitive to noise and consequently provides poor results. The number of false detections is important and the method is not sufficiently reliable. For those two reasons, it has been rapidly discarded.

We propose a novel approach that consists in decoupling the xy and the z detection. The xy detection is performed on the phase image $\phi(x,y)$ rather than the intensity one. The in-depth z detection is performed locally within a region of interest (ROI) surrounding each detected vesicle. Indeed, although the image of a vesicle undergoes strong changes in intensity while propagated along the z direction, it keeps a very slowly changing shape on the phase image. As an example, Fig. 3 compares the intensity and the phase image for one vesicle (diameter of about 20 µm) in three different planes (respectively −70 µm, 46µm – focus plane – and + 100 µm).

#206641 - $15.00 USD Received 18 Feb 2014; revised 10 Apr 2014; accepted 11 Apr 2014; published 17 Apr 2014
(C) 2014 OSA

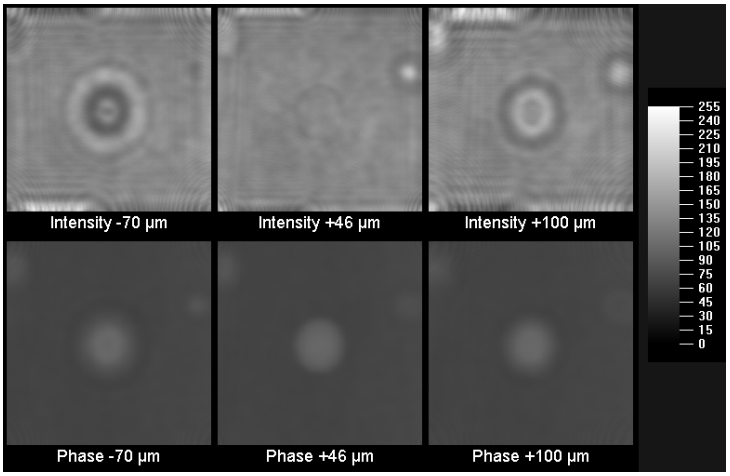

Fig. 3. Examples of intensity and phase images of a vesicle (diameter around 20 µm) at different planes (focus plane + 46 µm, at the middle and out of focus –70 µm and + 100 µm). Scalebar on the right indicates the grey levels.

Excepted for very small vesicles, a simple threshold on the phase image (corresponding to the focus plane of the microscope) detects almost all the vesicles. Nevertheless, due to phase jumps induced by the periodicity of the phase, one cannot work directly on the wrapped phase image. Usually, the phase map is unwrapped to get a continuous phase distribution. Unwrapping might be a tough task and is generally time consuming [46]. In our case, the phase change induced by vesicles is, excepted for very big vesicles (which are not considered in our study), below 2π. The removal of phase jumps can thus be easily made by subtracting (modulo 2π) the background phase [47]. Because of the symmetry between the reference and the object beam of the interferometer, we used a compensation method which consists in fitting the background phase with a bi-dimensional quadratic phase map. Due to phase jumps, the fitting cannot be performed directly on the phase image. For this reason, we perform the fitting on the derivative of the phase map [15,48]. Figure 4 illustrates the compensation method with a phase map (a), the fitted background map (b) and the subtracted phase map (or compensated phase map) (c).

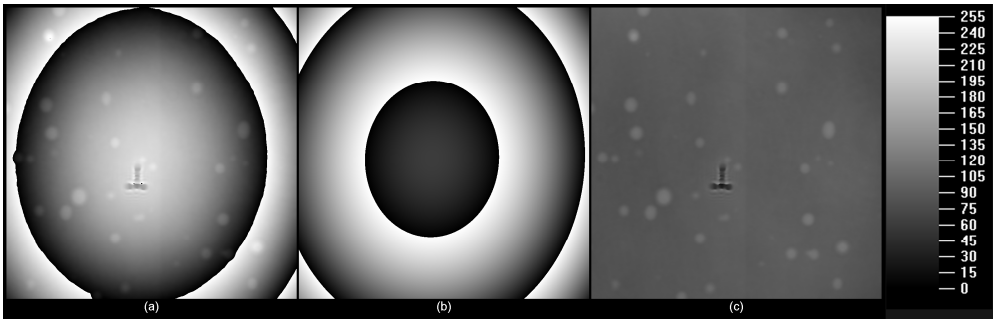

Fig. 4. Example of compensation. (a) original phase map; (b) fitted phase map; (c) compensated phase map. Scalebar on the right indicates the grey levels.

Unlike the original phase map, the compensated phase presents an almost uniform background on which vesicles appear as bright patches. This phase map compensation is indispensable as will be highlighted later for the extraction of geometrical features of vesicles. Nevertheless, the compensation method used here is based on a fitting and does not perfectly compensate the background phase. As a consequence, the compensated phase does not present a perfectly flat background allowing a simple threshold. Putting a threshold a little bit higher than the background value does not solve completely the problem as it might swallow

#206641 - $15.00 USD Received 18 Feb 2014; revised 10 Apr 2014; accepted 11 Apr 2014; published 17 Apr 2014

up small vesicles. We remove those background fluctuations (which can be of several grey levels) by subtracting the mean compensated phase image (computed on all the compensated phase maps of the sequence under processing – it corresponds to a minimum of 600 images). A simple filtering of the thresholded image removes the small local fluctuations that can be considered as false detections (we remove all the connected area smaller than 200 pixels which corresponds to vesicles having a diameter smaller than 6 µm). This detection method is very simple and presents several advantages. First, the detection is very fast and very efficient (more than 95% of the vesicles are correctly detected). Secondly, the proposed detection method performs a first segmentation of the vesicles which gives a rough determination of their size and shape. This point is very important for the *z* detection. Figure 5 shows an example of *xy* detection and pre-segmentation of the vesicles. Note that the smallest vesicles, correctly detected, present very low contrasts demonstrating the efficiency of the proposed method.

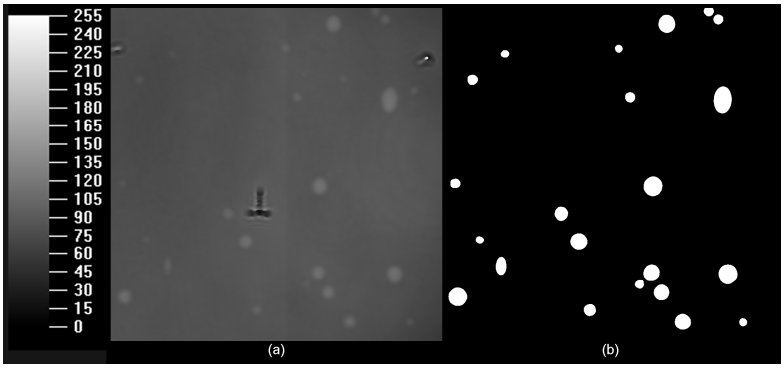

Fig. 5. Example of *xy* detection. (a) Original phase map. (b) *XY* detection and pre-segmentation of the vesicles. Scalebar on the left indicates the grey levels.

Once the *xy* position of each vesicle is known, the *z* detection is performed locally on a ROI centered on the vesicle. The complex amplitude and the corresponding compensated phase are cropped locally and the *z* scanning is performed using the numerical propagation inside this ROI. The dimensions of the ROI are determined by the pre-segmentation performed during the *xy* detection. We used ROIs whose dimensions equal twice the width and the height of the segmented vesicle. In this way, ROIs are selected differently for each vesicle, minimizing the dimensions of the Fourier Transforms needed for the numerical propagations. To avoid border diffractions due to the ROI borders, we extend the ROI size with values that minimize the borders diffraction [49]. In this way, the ROI is extended to the smallest value that fits the requirement of Fast Fourier Transforms (the size must be a power of 2). For example, for a vesicle whose width and height are respectively 80 and 105 pixels, we will crop the complex amplitude with an ROI of 160 x 210 pixels that will then be enlarged to 256 x 256 pixels. Considering enlarged ROI of 256 x 256 pixels, the numerical propagation inside ROI is faster than the whole hologram propagation as long as the number of vesicles present in the hologram is smaller than 88. For a larger number of vesicles, the whole hologram propagation becomes faster. Nevertheless, the highest concentrations studied didn't exceed 50 vesicles per hologram.

Digital Holography allows to numerically investigate a volume by refocusing the different slices but does not provide any information about the focus status. In [50], we have proposed a focus metrics based on the integral of the modulus of the complex amplitude. It has been shown that this metrics is maximal for phase objects when the reconstructed distance reaches the best focus plane. Nevertheless, this criterion is based on an integral and gives a value that is influenced by all the objects distributed in the volume. If, following the discussion of the previous paragraph, another vesicle is present in the ROI, the *z* value will be influenced by both vesicles and will give a mean value which does not correspond to the *z* position of any of the two vesicles (unless they are in the same plane). To cope with all those requirements, we

#206641 - $15.00 USD Received 18 Feb 2014; revised 10 Apr 2014; accepted 11 Apr 2014; published 17 Apr 2014
(C) 2014 OSA

use a mask that determines the region where the integral must be calculated. This mask is computed on the basis of the pre-segmented shape provided by the *xy* detection. We enlarge the pre-segmented shape by a border of 10 pixels (this value is chosen after successive trials). This is made simply by applying 10 times a dilatation operation. Indeed, it has been demonstrated [51] that the flux density of the complex amplitude distribution is proportional to the gradient of the complex amplitude, and consequently, its evolution direction is perpendicular to the object border during the propagation. Figure 6 shows an example of a vesicle with the different ROI considered and the mask defining the domain of integration.

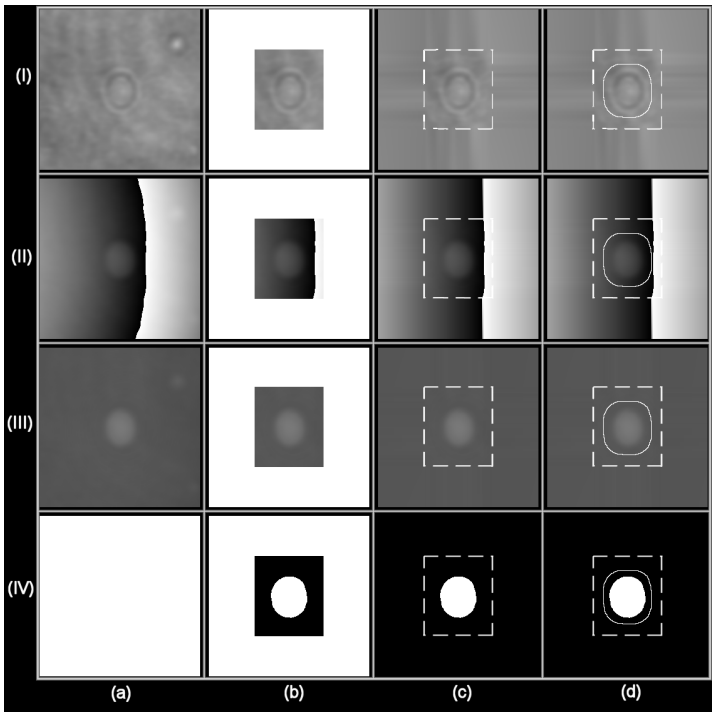

Fig. 6. Description of the different ROIs. Row (I): Intensity, Row (II): Phase, Row (III): Compensated phase, Row (IV): Mask. Col (a): Vesicle under consideration, Col (b): Cropped ROI (110 x 128 pixels) ; IV-b is the pre-segmented vesicle, Col(c): Enlarged ROI (256 x 256 pixels) with values minimizing the diffraction (cropped ROI in dashed line), Col (d): Contour line of the region where the metrics for the best focus plane is computed – cropped ROI in dashed line.

To illustrate the efficiency of the processing, Fig. 7 shows an example of a region containing 4 vesicles with close *xy* position but different *z* positions. Table 1 describes the different positions (and the equivalent diameters) of the 4 vesicles.

#206641 - $15.00 USD Received 18 Feb 2014; revised 10 Apr 2014; accepted 11 Apr 2014; published 17 Apr 2014
(C) 2014 OSA

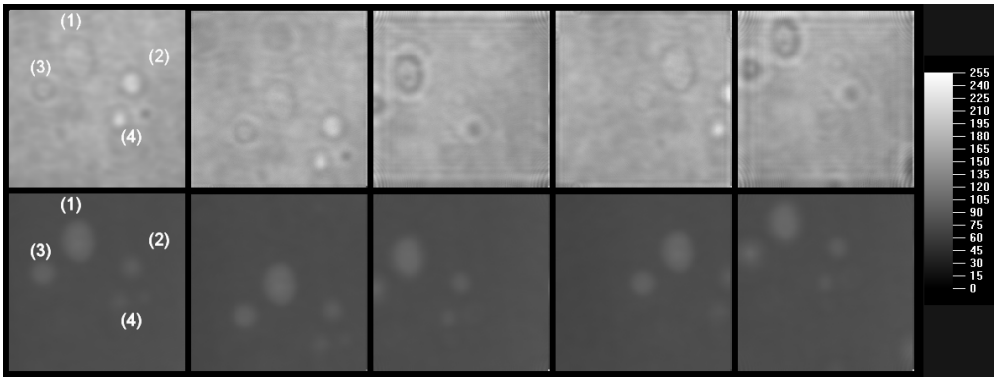

Fig. 7. Example of 4 vesicles with close *xy* position and different *z* positions. First row: intensity image, second row: compensated phase image. First column: identification of the 4 vesicles (ROI 210 x 210 pixels), column 2 to 5 correspond to vesicle 1 to 4 (ROI cropped around the center of each vesicle). Scalebar on the right indicates the grey levels.

Table 1. XYZ position and equivalent diameter of the 4 vesicles of Fig. 7.

	Position X	Position Y	Position Z	Diameter
Vesicle 1	129.2 µm	109.1 µm	–1.9 µm	16.6 µm
Vesicle 2	155.8 µm	122.2 µm	–31.2 µm	10.0 µm
Vesicle 3	112.8 µm	125.1 µm	+ 7.2 µm	11.8 µm
Vesicle 4	149.7 µm	139.4 µm	–35.2 µm	6.2 µm

Of course, when the distance between two (or more) vesicles is too small, it becomes impossible to consider them separately and the discussion above fails into default. We will see in the next subsection how to remove those occurrences from the output data.

The processing time is directly linked to the increment Δz used when propagating the cropped amplitude along the *z* axis but determines also the accuracy on the *z* axis. Decreasing Δz will increase the accuracy of the measured *z* position but will also increase the processing time. Instead of using a dichotomous approach, we take benefit of a previous theoretical analysis of this metrics [52]. Indeed, it has been demonstrated that around the focus point, the curve of the integrated modulus of the complex amplitude was of parabolic shape. The accuracy is then obtained by fitting the curve with a parabola around the maximum. The best focus plane is then derived analytically using the fitting parameters. In this way, we can use larger increment Δz while keeping a high accuracy in *z*. In the experiments, we propagate numerically along *z* over 180 µm (covering the thickness of the experimental cell) with an increment Δz of 5 µm. The parabolic fitting is performed on 9 points equally distributed around the curve maximum. In this way, we obtain an accuracy along *z* of 1 µm (which is much better than the classical depth of focus of 6 µm). This accuracy is determined by measuring, with the same setup, the standard deviation of the linear-fitted curve $z(t)$ of the sedimentation of a vesicle (which is linear in time).

4.2 Feature extraction

The *xyz* position of each vesicle obtained, size and shape must be determined. For this purpose, vesicles must be segmented on the phase map in order to delimit their border. The pre-segmentation obtained during the *xy* detection is rough and not sufficiently precise to get reliable parameters of the shape. This is due to the fact that the pre-segmentation is performed in the focus plane of the microscope which is, most of the time, not the one of the vesicles (see for example Fig. 7). The compensated phase is thus propagated to the corresponding *z* plane before to be segmented.

Boundaries of vesicles are smooth and require more sophisticated segmentation techniques like active contours for feature extraction. Active contour techniques are iterative processes that attempt to minimize a defined function and are much more suitable for applications with

#206641 - $15.00 USD Received 18 Feb 2014; revised 10 Apr 2014; accepted 11 Apr 2014; published 17 Apr 2014

smooth boundaries. Starting from an initial contour centered on the object, the successive iterations deform the contour until the function is minimized and the deformed contour fits the boundaries of the object. We used an active contour algorithm based on the Mumford-Shah functional minimization [53]. Our motivation for choosing the active contour technique is guided by the following: we know the position (*x,y*) of the object and its approximate shape (from the pre-segmentation), around which we have cropped the ROI. Thus, as an initial contour, we can reasonably choose a circle with a diameter extracted from the pre-segmentation. In this way, the processing time of the segmentation is drastically reduced and much more reliable as the Mumford-Shah algorithm is very sensitive to the initial contour. The segmentation process delimits the boundaries of the vesicle. Feature extraction is then performed by fitting the segmentation contour with an ellipse. Size of vesicles is given by the big and small axis (respectively a_1 and a_2) of the fitted ellipse. Shape is given by the aspect ratio $AR = a_1/a_2$ related to the deflation of the vesicle [14]. Figure 8 illustrates the segmentation and feature extraction process of two vesicles of almost the same equivalent diameter (around 20 µm) but different deflations.

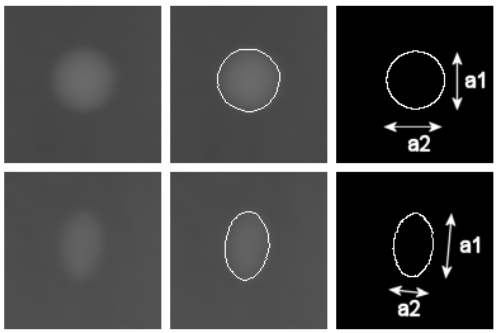

Fig. 8. Example of two vesicles with equivalent diameter (around 20 µm) but different deflations. First column: vesicle 1 and 2. Second column: Segmented vesicles (segmentation contour in white). Third column: corresponding fitted ellipse (a1 is the big axis, a2 is the small axis).

Table 2 describes the different parameters of Fig. 8. As we can see, other parameters are extracted from the fitted ellipse such as the orientation of the big axis with respect to the flow direction (from top to bottom of the images) and the mean square error of the fitting. Orientation should be considered only for elliptical vesicles with an aspect ratio different of 1. Those additional parameters are useful to detect and remove false detections (like aggregates) or segmentation errors (mainly on the smallest and very low contrasted vesicles). Figure 9 shows example of false detections.

Table 2. Parameters extracted from the segmentation process of Fig. 8. MSE is the Mean Square Error.

	Pos. z	Big axis a_1	Small axis a_2	Aspect Ratio	Orientation	MSE
Vesicle 1	45.91 µm	19.2 µm	18.9 µm	1.02	172.6 °	0.6 µm
Vesicle 2	−5.9 µm	20.9 µm	13.1 µm	1.59	4.77 °	0.5 µm

#206641 - $15.00 USD Received 18 Feb 2014; revised 10 Apr 2014; accepted 11 Apr 2014; published 17 Apr 2014

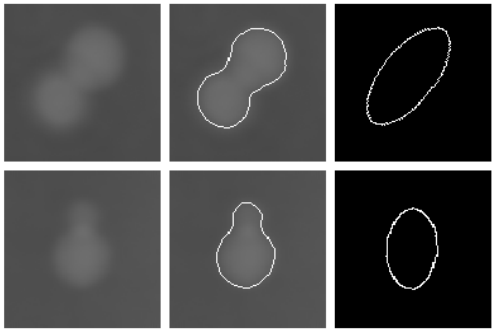

Fig. 9. Example of false detections. First column: vesicle 1 and 2. Second column: Segmented vesicles (segmentation contour in white). Third column: corresponding fitted ellipse. Aggregate of first line: Orientation = 38.57°, MSE = 1.34 µm, AR = 2.16. Aggregate of second line: Orientation = 3.21°, MSE = 1.12 µm, AR = 1.61.

In the results presented in the following section, we have considered as false detections, MSE values above 1.1 µm. This value has been determined by selecting manually 100 different false detections and among those, measuring the smallest MSE. Further filtering of the data has been made on the orientation by removing orientations bigger than 15° when the AR exceeds 1.3. Indeed, the measurement of the orientation is relevant only for significantly deflated vesicles, whose long axis should be aligned with the flow direction. If this not the case, the detected object is an aggregate as depicted in the first row of Fig. 9. By this procedure, and depending on the concentration of the sample, we discard up to 5% of the data but strongly increase the reliability. Note that specific methods exist to process and separate aggregates [51,54]. Nevertheless, we did not implement them since for our study only the dynamics of single vesicles is considered and the reliability criterion consists in ensuring that no false detection is made. Tracking of individual vesicles is not of interest in our case as we are essentially interested in the description of the temporal evolution of the suspension. Obtaining the trajectories of individual vesicles would become meaningful for a deeper study of the diffusion process. However, this would require a much higher frame rate and a different setup, since in the range of shear rates explored, the velocity of vesicles is of order a few mm/s and the field of view only 0.37 mm long, which does not allow observing a significant portion of individual vesicle trajectories or even interaction processes.

Applying the processing presented in the two previous sub-sections on all the holograms of an experiment results in a 4D distribution describing the evolution of the tri-dimensional distribution. From this data, physical properties of the suspension can be extracted such as the lift velocity, shear-induced diffusion, population … Note that this algorithm is not restricted to vesicles and has been successfully applied for RBC dynamics under shear flow [55].

5. Illustrative examples

The hydrodynamic interactions between deformable particles and walls or other particles strongly depend not only on their size but also on their ability to deform. For objects with incompressible membranes, such as lipid vesicles or red blood cells, this ability strongly depends on their initial volume over surface ratio, which stays constant in time under flow. At rest, the excess area may however not be visible: the bending modulus is typically of order a few kT, which favors local folding of the membrane. The characterization of deflation within a given population therefore need to be done under flow. In simple shear flow, vesicles adopt an ellipsoidal shape whose main axis is in the shear plane *(xy)*. Our analysis provides the small axis a_2 in the vorticity direction *(z)* as well as the apparent long axis a_1 in the flow direction *(x)*, which is the long axis of the projection of the vesicle shape onto the *(xz)* plane. The ratio a_1/a_2 characterizes the deflation of the vesicle. On Figs. 10 and 11, we show the size and apparent aspect ratio distribution within a vesicle suspension. Electroformation method provides a vesicle suspension with a strong size disparity. This suspension was sorted out

#206641 - $15.00 USD Received 18 Feb 2014; revised 10 Apr 2014; accepted 11 Apr 2014; published 17 Apr 2014

thanks to a pinched flow fractionation method [56,57] and two subpopulations were mixed as to get a bi-disperse suspension. The distribution was extracted from a sequence of 1476 holograms in which 24362 vesicles were correctly detected. Depending on the size of the vesicles, the processing times may slightly vary. In average, on a recent processor, the algorithm processes between 700 and 800 vesicles per hour. Note that the process can be easily spread on multiprocessor platforms.

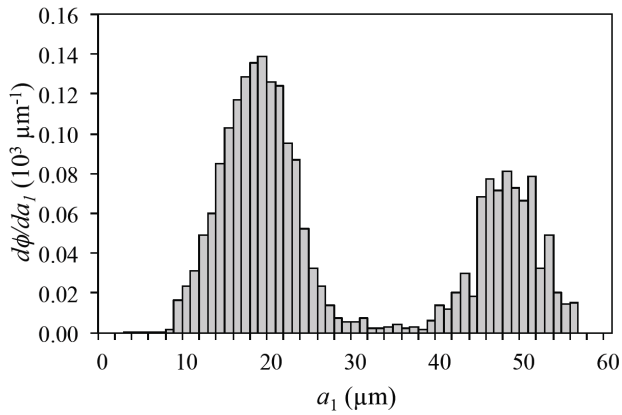

Fig. 10. Size distribution within a vesicle suspension under shear: volume fraction density as a function of apparent long axis a_1 .

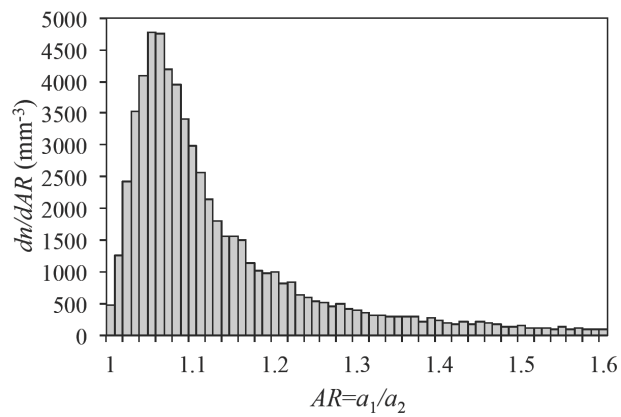

Fig. 11. Aspect ratio a_1/a_2 distribution in the vesicle suspension of Fig. 10.

An evolution of the *z* position of all vesicles in the field of view along a shearing experiment is shown on Figs. 12 and 13. The data was extracted from two sequences of 600 holograms in which 2257 (Fig. 12) and 7575 (Fig. 13) vesicles were correctly detected. The vesicles initially lay on the bottom plate and are sheared during a microgravity phase, so that only hydrodynamic interactions between themselves and with the walls are present. The initial lift-off stage where the top plate is too far to play a role was described in a preceding paper [14] and is in agreement with several numerical and theoretical papers [27,31,36]. Lift velocity decreases with distance to the wall with a power law with exponent *-2*. At longer time, vesicles start to feel the influence of the top plate and eventually reach, on average, the middle plane of the cell. As shown on the graphs, this mean behavior is well described by assuming that the effects of both walls are additive, so that the mean velocity along the *(z)* axis scales as $1/z^2-1/(h-z)^2$. As the vesicles migrate towards the center, their distribution broadens. This diffusion cannot be a Brownian diffusion due to the large size of the vesicles, but it is due to the multiple interactions between the vesicles. For not too large concentrations,

#206641 - $15.00 USD Received 18 Feb 2014; revised 10 Apr 2014; accepted 11 Apr 2014; published 17 Apr 2014

pair interactions are predominant, so that the diffusion constant depends linearly on concentration [55,58]. This implies in particular that the width should increase with time following a power law with exponent *1/3* [55,59]. This is illustrated on Fig. 14, where standard deviations in the vesicle distribution are plotted as a function of time.

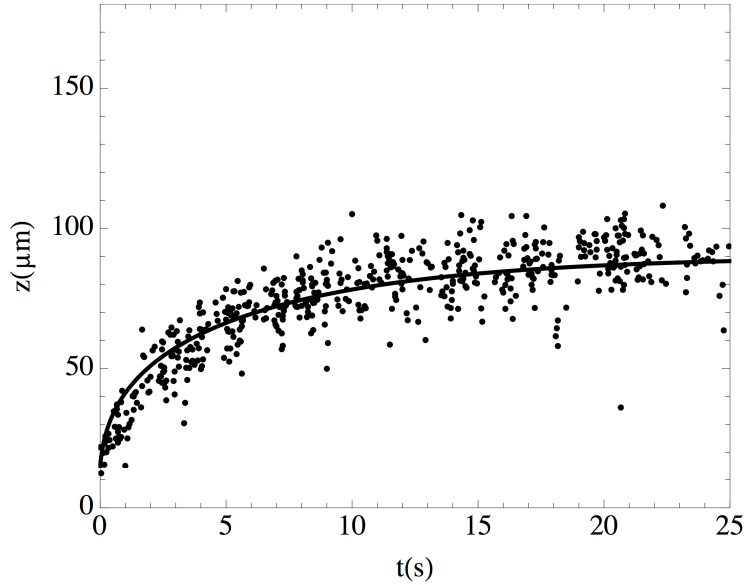

Fig. 12. *z* positions of vesicles across the shear chamber of thickness $h = 170$ microns. Shear rate is 50 s^{-1} and volume concentration $1.9x10^{-3}$ Vesicles were sorted by pinched flow fractionation method, so that $a_1 = 16 \pm 3$ microns. Only vesicles with AR between 1.1 and 1.3 are represented. Quasi-spherical vesicles lift much less. More deflated vesicles are rare (see Fig. 11). The full line shows the one parameter fit by the $z(t)$ evolution obtained by solving $dz/dt = A\,(1/z^2 - 1/(h-z)^2)$.

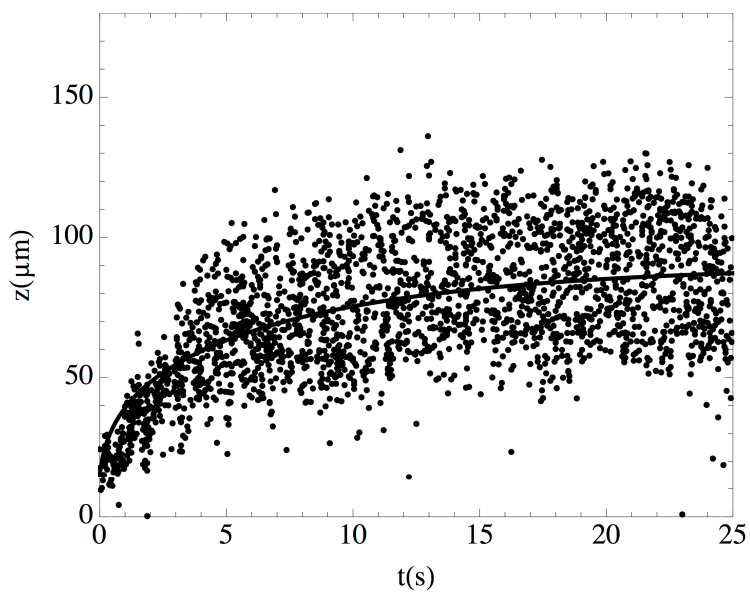

Fig. 13. Same as Fig. 12 but with volume concentration $7.2x10^{-3}$.

#206641 - $15.00 USD Received 18 Feb 2014; revised 10 Apr 2014; accepted 11 Apr 2014; published 17 Apr 2014

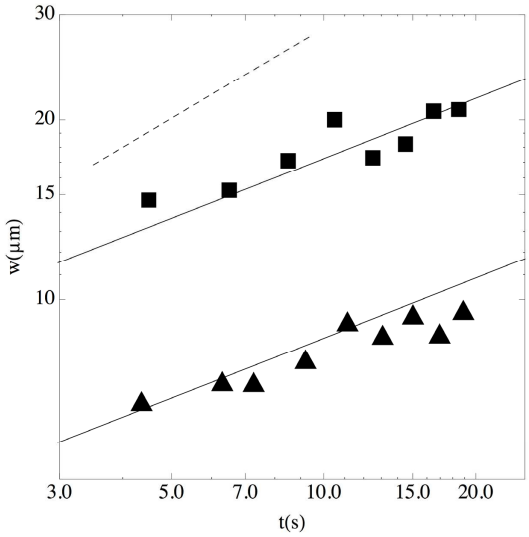

Fig. 14. Time evolution of the standard deviation *w* in the distribution of vesicles for the two clouds of Figs. 12 (triangles) and 13 (squares), in log-log scale. Full lines have slopes *1/3* while the dotted line has slope *1/2*.

These examples demonstrate the accuracy of our procedure and will be embedded in a more complete set of data and theoretical modeling to be presented elsewhere, where the diffusion coefficients will be determined, as well as the cross-diffusion coefficients in the case of a bi-disperse suspension.

6. Conclusions

In this paper, we have proposed a fully automated processing of digital holograms for monitoring the dynamics of a vesicle suspension under shear flow. The understanding of complex fluids in confined flows is of importance as they have direct consequences on the rheology of biological fluids like blood and especially on the transport of oxygen by red blood cells in the smallest capillaries. The novel approach presented combines in elegant way different holographic techniques while keeping reasonable processing times with a good reliability. Automated detection is most of the time problem dependant, especially when we add the in-depth dimension. We separated the tri-dimensional detection by an in-plane followed by an in-depth detection. This approach presents several advantages notably a pre-segmentation of the objects indispensable for a good in-depth detection and feature extraction. Experimental results show a very good agreement with theoretical models demonstrating that DHM coupled with the proposed method is an adequate and powerful tool for studying complex fluids.

Acknowledgments

The authors acknowledge financial support from the European Space Agency (ESA) and Centre National d'Etudes Spatiales (CNES) and access to microgravity platforms (Sounding Rockets and parabolic flights). This work was supported by the SSTC/ESA-PRODEX contract 90171.